

Geometrical scaling for energies available at the BNL Relativistic Heavy Ion Collider to those at the CERN Large Hadron Collider

M.Petrovici,^{1,2} A.Lindner,^{1,2} A.Pop,¹ M.Târzișă,^{1,2} and I.Berceanu¹

¹*National Institute for Physics and Nuclear Engineering - IFIN-HH
Hadron Physics Department
Bucharest - Romania*

²*Faculty of Physics, University of Bucharest*

(Dated: November 17, 2021)

Based on the recent RHIC and LHC experimental results, the $\langle p_T \rangle$ dependence of identified light flavour charged hadrons on $\sqrt{\langle \frac{dN}{dy} \rangle / S_\perp}$, relevant scale in gluon saturation picture, is studied from $\sqrt{s_{NN}}=7.7$ GeV up to 5.02 TeV. This study is extended to the slopes of the $\langle p_T \rangle$ dependence on the particle mass and the $\langle \beta_T \rangle$ parameter from Boltzmann-Gibbs Blast Wave (BGBW) fits of the p_T spectra. A systematic decrease of the slope of the $\langle p_T \rangle$ dependence on $\sqrt{\langle \frac{dN}{dy} \rangle / S_\perp}$ from BES to the LHC energies is evidenced. While for the RHIC energies, within the experimental errors, the $\langle p_T \rangle / \sqrt{\langle \frac{dN}{dy} \rangle / S_\perp}$ does not depend on centrality, at the LHC energies a deviation from a linear behaviour is observed towards the most central collisions. The influence of the corona contribution to the observed trends is discussed. The slopes of the $\langle p_T \rangle$ particle mass dependence and the $\langle \beta_T \rangle$ parameter from BGBW fits scale well with $\sqrt{\langle \frac{dN}{dy} \rangle / S_\perp}$. Similar systematic trends for pp at $\sqrt{s}=7$ TeV are in a good agreement with the ones corresponding to Pb-Pb collisions at $\sqrt{s_{NN}}=2.76$ TeV and 5.02 TeV pointing to a system size independent behaviour.

PACS numbers: 25.75Ag, 25.75Ld, 25.75Nq, 21.65.Qr

I. INTRODUCTION

Parton density evolution as a function of x and Q^2 , addressed more than 35 years ago [1] and its experimental confirmation at HERA [2] have triggered a real interest in the community studying ultra-relativistic heavy ion collisions. The rise of the structure function at low x , still visible at small values of Q^2 [3, 4] where the perturbative QCD does not work anymore, requires new approaches for a complete understanding of the $\log \frac{1}{x} - \log Q^2$ QCD landscape. Low x values and moderate Q^2 are characteristic features for the early stage of hadron collisions starting from RHIC up to LHC energies. For average transverse momentum ($\langle p_T \rangle$) values of the order of 1-2 GeV/c, specific for this range of energies, the x values at mid rapidity are of the order of $\sim 10^{-2}$ and $\sim 10^{-4}$ respectively. Such initial conditions are used by different theoretical approaches for describing especially the most recent results from LHC energies. Colour Glass Condensate (CGC) is one of such approaches based on strong classical colour fields description of the small x degrees of freedom [5–7]. Local parton-hadron duality picture (LPHD) [8] and dimensionality argument [9, 10] predict a decrease of the ratio between the average transverse momentum and the square root of the hadron multiplicity per unit of rapidity and unit of the colliding hadrons transverse overlapping area ($\langle p_T \rangle / \sqrt{\langle \frac{dN}{dy} \rangle / S_\perp}$) towards central collisions and higher energies. With the latest results from the Beam Energy Scan (BES) at RHIC and the highest energies at LHC, it is worth revisiting such a dependence. Recently evidenced similarities between pp, p-Pb and Pb-Pb collisions at LHC energies in terms of long

range near side two particle correlations, transverse flow and strangeness enhancement as a function of charged particle multiplicity [11–17] support the idea that even in small colliding systems, due to increased parton density at such energies, the probability of multiple parton interaction increases, the rescattering processes become important and a thermalised stage could be reached although the interaction time is extremely short. Such a high density deconfined small system could follow a hydrodynamic type expansion. To what extent the hydrodynamics is applicable in small systems is still under debate [18]. The most successful phenomenological models, UrQMD, HIJING, NeXSPheRIO, AMPT, PHSD, EPOS, describing the latest results obtained at LHC in pp, p-Pb and Pb-Pb collisions are based on combinations of different approaches for different stages of the collision [19–24] while the classical phenomenological models used in particle physics like PYTHIA [25], HERWIG [26] and PHOJET [27] had to implement processes like multiparton interaction, rescattering, colour reconnection [28] or shoving mechanism [29] in order to improve the agreement with the LHC results, especially in the soft sector in pp collisions. In this paper we also present a comparison between pp and Pb-Pb at LHC energies in terms of the dependence of different observables on the $\sqrt{\langle \frac{dN}{dy} \rangle / S_\perp}$ variable. In the second chapter of the paper the estimates of the overlapping area of the colliding hadrons are presented. Details on the hadron density per unit of rapidity are given in the third chapter. The $\langle p_T \rangle$ dependence on $\sqrt{\langle \frac{dN}{dy} \rangle / S_\perp}$ is presented in Chapter IV for BES and $\sqrt{s_{NN}}=62.4, 130, 200$ GeV Au-Au collisions measured by the STAR Collaboration at RHIC and for Pb-

Pb collisions at $\sqrt{s_{NN}}=2.76$ and 5.02 TeV measured by the ALICE Collaboration at LHC. Chapter V is dedicated to the $\sqrt{(dN/dy)/S_{\perp}}$ dependence of the slope of the linear $\langle p_T \rangle$ versus particle mass behaviour for identified light flavour charged hadrons. The BGBW fit parameters of p_T spectra are presented versus the same geometrical variable of the colliding systems in Chapter VI. Similarities, in terms of $\sqrt{(dN/dy)/S_{\perp}}$ dependence of different observables, in pp at $\sqrt{s}=7$ TeV and Pb-Pb at $\sqrt{s_{NN}}=2.76$ and 5.02 TeV are discussed in Chapter VII. Chapter VIII is dedicated to conclusions.

II. OVERLAPPING AREA S_{\perp} ESTIMATES

The overlapping area of the two colliding nuclei for a given incident energy and centrality was estimated based on the Glauber Monte Carlo (GMC) approach [30–33]. For the nuclear density profile of the colliding nuclei, a Wood-Saxon distribution was considered:

$$\rho(r) = \frac{1}{1 + \exp(\frac{r-r_0}{a})} \quad (1)$$

with $a=0.535$ fm, $r_0=6.5$ fm for the Au nucleus [34] and $a=0.546$ fm, $r_0=6.62$ fm for the Pb nucleus [35]. Within the black disc approach, the nucleons are considered to collide if the relative transverse distance $d \leq \sqrt{\frac{\sigma_{pp}}{\pi}}$, where σ_{pp} is the nucleon-nucleon interaction cross section. The σ_{pp} values for the corresponding $\sqrt{s_{NN}}$ energies were taken from [34–37]. The main characteristics of the collision at different centralities for Au-Au at $\sqrt{s_{NN}}=7.7, 11.5, 19.6, 27$ and 39 GeV obtained in the Beam Energy Scan (BES) at RHIC [38], Au-Au at $\sqrt{s_{NN}}=62.4, 130$ and 200 GeV [34] and Pb-Pb at $\sqrt{s_{NN}}=2.76$ and 5.02 TeV [35, 37] are presented in Table I (see caption for notations). The geometrical overlapping areas (S_{\perp}^{geom}) have been estimated by averaging the maximum values of the x and y coordinates determined per event, over many events. S_{\perp}^{var} has been estimated as being proportional to the quantity $S = \sqrt{\langle \sigma_x^2 \rangle \langle \sigma_y^2 \rangle - \langle \sigma_{xy} \rangle^2}$, σ_x^2, σ_y^2 are the variances and σ_{xy} is the co-variance of the participant distributions in the transverse plane, per event [39]. They were averaged ($\langle \dots \rangle$) over many events.

System	$\sqrt{s_{NN}}$ (GeV)	Cen. (%)	$\langle N_{part} \rangle$	S_{\perp}^{geom} (fm^2)	S_{\perp}^{var} (fm^2)	f_{core}	$(S_{\perp}^{geom})^{core}$ (fm^2)	$(S_{\perp}^{var})^{core}$ (fm^2)	dN/dy
Au-Au	7.7	0-5	337±2	146.1±0.7	147.1±0.7	0.88±0.00	126.5±0.6	124.6±0.6	476.7±22.5
		5-10	290±6	126.9±0.7	129.7±0.6	0.84±0.00	107.6±0.7	105.0±0.5	392.5±18.5
		10-20	226±8	103.6±0.7	108.9±0.5	0.80±0.00	85.5±0.7	84.3±0.4	295.4±14.0
		20-30	160±10	79.7±0.8	87.1±0.4	0.75±0.00	63.3±0.7	63.8±0.3	203.6±9.8
		30-40	110±11	61.2±0.8	70.4±0.3	0.70±0.00	46.6±0.7	48.9±0.2	135.1±6.4
		40-50	72±10	45.9±0.8	56.9±0.3	0.63±0.00	33.1±0.8	37.5±0.2	84.8±4.1
		50-60	45±9	32.8±0.8	45.7±0.2	0.56±0.00	21.9±0.8	28.9±0.1	51.5±2.5
		60-70	26±6	21.8±0.8	36.3±0.2	0.47±0.00	12.8±0.7	22.6±0.1	27.6±1.4
		70-80	14±4	12.1±0.7	26.8±0.2	0.37±0.00	5.4±0.6	15.6±0.1	13.8±0.8
Au-Au	11.5	0-5	338±2	146.1±0.7	147.1±0.7	0.88±0.00	126.5±0.6	124.5±0.6	565.1±29.5
		5-10	291±6	126.6±0.7	129.5±0.6	0.84±0.00	107.2±0.7	104.6±0.5	449.0±23.3
		10-20	226±8	103.5±0.7	108.9±0.5	0.80±0.00	85.3±0.7	84.1±0.4	335.5±17.5
		20-30	160±9	79.9±0.8	87.3±0.4	0.75±0.00	63.4±0.7	63.9±0.3	225.5±11.8
		30-40	110±10	61.3±0.8	70.5±0.3	0.70±0.00	46.6±0.7	48.9±0.2	152.0±8.1
		40-50	73±10	45.8±0.8	56.9±0.3	0.63±0.00	33.0±0.8	37.5±0.2	94.5±5.1
		50-60	44±9	32.9±0.8	45.9±0.2	0.56±0.00	21.9±0.8	28.9±0.1	55.8±3.1
		60-70	26±7	21.8±0.8	36.4±0.2	0.47±0.01	12.8±0.7	22.6±0.1	31.3±1.8
		70-80	14±6	12.1±0.7	26.8±0.2	0.37±0.01	5.4±0.6	15.5±0.1	16.0±0.9
Au-Au	19.6	0-5	338±2	146.6±0.7	147.5±0.7	0.89±0.00	126.9±0.6	125.0±0.6	683.4±40.0
		5-10	289±6	127.2±0.7	129.9±0.6	0.85±0.00	107.6±0.7	105.1±0.5	556.5±32.3
		10-20	225±9	104.0±0.7	109.4±0.5	0.81±0.00	85.6±0.7	84.5±0.4	421.7±24.7
		20-30	158±10	80.2±0.8	87.7±0.4	0.76±0.00	63.6±0.7	64.2±0.3	284.3±16.6
		30-40	108±11	61.4±0.8	70.7±0.3	0.70±0.00	46.6±0.7	49.0±0.2	187.9±11.1
		40-50	71±10	46.0±0.8	57.1±0.3	0.64±0.00	33.0±0.8	37.5±0.2	117.3±7.0
		50-60	44±9	32.9±0.8	45.9±0.2	0.56±0.00	21.8±0.8	28.8±0.1	70.3±4.2
		60-70	25±7	21.9±0.8	36.6±0.2	0.47±0.01	12.9±0.7	22.7±0.1	38.1±2.3
		70-80	14±5	12.1±0.5	26.7±0.2	0.37±0.01	5.4±0.6	15.5±0.1	19.8±1.3
Au-Au	27	0-5	343±2	147.2±0.7	148.3±0.7	0.89±0.00	127.6±0.6	125.8±0.6	727.0±42.2
		5-10	299±6	127.8±0.7	130.9±0.6	0.85±0.00	108.1±0.7	105.9±0.5	605.7±35.2
		10-20	234±9	104.6±0.7	110.2±0.5	0.81±0.00	85.9±0.7	85.1±0.4	457.6±26.6
		20-30	166±11	80.7±0.8	88.4±0.4	0.76±0.00	63.8±0.7	64.6±0.3	309.6±18.1
		30-40	114±11	61.9±0.8	71.3±0.3	0.71±0.00	46.8±0.7	49.3±0.2	203.6±11.9
		40-50	75±10	46.1±0.8	57.4±0.3	0.64±0.00	33.1±0.8	37.6±0.2	128.2±7.6
		50-60	47±9	32.9±0.8	46.1±0.2	0.56±0.00	21.7±0.8	28.8±0.1	76.0±4.5
		60-70	27±8	21.9±0.8	36.6±0.2	0.47±0.01	12.8±0.7	22.5±0.1	41.9±2.3
		70-80	14±6	12.8±0.7	27.5±0.2	0.38±0.01	5.9±0.6	16.3±0.1	20.4±1.3

Au-Au	39	0-5	342±2	147.9±0.7	149.2±0.7	0.89±0.00	128.4±0.6	126.7±0.6	756.2±44.1
		5-10	294±6	128.4±0.7	131.7±0.6	0.86±0.00	108.6±0.7	106.6±0.5	633.0±36.8
		10-20	230±9	104.9±0.7	110.8±0.5	0.81±0.00	86.2±0.7	85.6±0.4	482.2±28.2
		20-30	162±10	81.0±0.8	89.0±0.4	0.76±0.00	64.0±0.7	65.0±0.3	328.2±19.1
		30-40	111±11	62.2±0.8	71.9±0.3	0.71±0.00	47.1±0.7	49.7±0.2	215.6±12.5
		40-50	74±10	46.6±0.8	58.0±0.3	0.65±0.00	33.3±0.8	37.9±0.2	136.3±7.9
		50-60	46±9	33.4±0.8	46.6±0.2	0.57±0.00	22.1±0.8	29.0±0.1	82.9±4.8
		60-70	26±7	22.1±0.8	36.8±0.2	0.48±0.01	12.9±0.7	22.5±0.1	44.9±2.6
70-80	14±5	12.8±0.7	27.5±0.2	0.38±0.01	5.8±0.6	16.1±0.1	23.5±1.5		
Au-Au	62.4	0-5	346.5±2.8	148.9±0.7	150.1±0.7	0.90±0.00	129.1±0.6	127.6±0.6	952.8±37.7
		5-10	293.9±4.2	129.3±0.7	132.8±0.6	0.86±0.00	109.1±0.7	107.4±0.5	780.9±28.7
		10-20	229.8±4.6	105.7±0.8	111.9±0.5	0.82±0.00	86.4±0.7	86.3±0.4	588.1±24.0
		20-30	164.1±5.4	81.5±0.8	89.9±0.4	0.77±0.00	64.1±0.7	65.4±0.3	406.4±15.3
		30-40	114.3±5.1	62.6±0.8	72.6±0.3	0.72±0.00	47.1±0.2	49.9±0.2	270.3±11.2
		40-50	76.3±5.2	47.0±0.8	58.7±0.3	0.65±0.00	33.4±0.7	38.1±0.1	174.4±7.6
		50-60	47.9±4.7	33.7±0.8	47.1±0.2	0.58±0.00	22.2±0.8	29.1±0.1	105.5±5.1
		60-70	27.8±3.7	22.3±0.8	37.1±0.2	0.48±0.01	12.9±0.8	22.4±0.1	58.2±2.8
70-80	15.3±2.4	12.9±0.7	27.5±0.2	0.38±0.01	5.8±0.7	15.9±0.1	28.4±1.3		
Au-Au.	130	0-6	344.3±3.1	148.4±0.7	150.3±0.7	0.90±0.00	128.6±0.7	127.4±0.6	1140.8±43.9
		6-11	289.0±5.4	127.3±0.7	131.8±0.6	0.86±0.00	106.8±0.7	106.0±0.5	920.6±35.1
		11-18	237.8±6.8	108.7±0.7	115.3±0.5	0.83±0.00	88.9±0.7	89.1±0.4	751.0±34.9
		18-26	187.7±7.5	89.5±0.8	97.8±0.4	0.79±0.00	71.0±0.7	72.4±0.3	569.3±24.2
		26-34	141.9±8.4	72.6±0.8	82.3±0.4	0.75±0.00	55.6±0.7	58.2±0.3	371.3±17.6
		34-45	100.9±8.4	56.0±0.8	67.2±0.3	0.70±0.00	40.9±0.8	44.9±0.2	246.0±11.0
		45-58	61.0±7.8	38.7±0.8	51.9±0.3	0.61±0.00	26.2±0.8	32.4±0.2	131.6±7.6
		58-85	22.6±5.0	16.3±0.8	31.5±0.2	0.43±0.01	8.2±0.8	17.7±0.1	39.9±4.3
Au-Au	200	0-5	350.6±2.4	150.9±0.7	152.4±0.7	0.92±0.00	131.2±0.7	130.3±0.6	1335.8±57.1
		5-10	298.6±4.1	131.6±0.7	136.0±0.6	0.88±0.00	110.9±0.7	110.4±0.5	1068.8±45.2
		10-20	234.3±4.6	108.1±0.8	115.3±0.5	0.83±0.00	88.1±0.7	89.1±0.4	797.2±33.5
		20-30	167.6±5.4	83.6±0.8	93.0±0.4	0.79±0.00	65.4±0.7	67.8±0.3	553.6±22.2
		30-40	117.1±5.2	64.6±0.8	75.5±0.4	0.73±0.00	48.3±0.8	51.9±0.2	365.2±15.1
		40-50	78.3±5.3	48.3±0.8	60.8±0.3	0.68±0.00	34.1±0.8	39.2±0.2	238.9±9.9
		50-60	49.3±4.7	34.9±0.8	48.9±0.2	0.59±0.00	22.8±0.8	29.7±0.1	147.8±5.9
		60-70	28.8±3.7	23.8±0.8	39.1±0.2	0.51±0.01	13.9±0.8	22.7±0.1	85.2±3.5
70-80	15.7±2.6	13.2±0.8	28.2±0.2	0.40±0.00	6.2±0.7	15.2±0.1	42.6±1.8		
Pb-Pb	2760	0-5	382.5±3.1	166.9±0.7	170.7±0.7	0.94±0.00	146.0±0.7	148.0±0.6	2837.0±144.0
		5-10	329.4±4.9	146.1±0.7	154.7±0.6	0.90±0.00	121.9±0.7	126.5±0.6	2345.5±112.4
		10-20	259.9±2.9	119.8±0.8	132.4±0.6	0.86±0.00	96.3±0.7	102.7±0.6	1763.2±84.8
		20-30	185.4±3.9	92.9±0.8	107.5±0.5	0.81±0.00	71.5±0.8	78.4±0.3	1195.8±54.2
		30-40	128.1±3.3	71.4±0.8	87.2±0.4	0.76±0.00	52.4±0.8	59.7±0.2	784.8±35.9
		40-50	84.2±2.6	53.7±0.8	70.3±0.3	0.70±0.00	37.2±0.8	44.8±0.2	482.7±21.4
		50-60	52.1±2.0	38.6±0.8	56.1±0.3	0.63±0.00	24.7±0.9	33.1±0.1	274.8±12.5
		60-70	29.5±1.3	25.7±0.8	43.6±0.2	0.54±0.00	14.6±0.9	23.8±0.1	141.8±5.4
70-80	14.9±0.6	14.2±0.8	30.8±0.2	0.43±0.00	6.4±0.7	15.1±0.1	67.2±3.0		
Pb-Pb	5020	0-5	385±2	170.2±0.7	174.2±0.7	0.94±0.00	149.0±0.7	151.5±0.6	3320.6±131.4
		5-10	333±4	149.2±0.7	158.5±0.6	0.90±0.00	124.4±0.7	129.9±0.5	2698.7±117.2
		10-20	263±4	122.4±0.8	135.8±0.6	0.86±0.00	98.1±0.7	105.6±0.4	2042.5±84.7
		20-30	188±3	94.9±0.8	110.5±0.5	0.82±0.00	72.9±0.7	80.8±0.3	1401.4±62.9
		30-40	131±2	73.4±0.8	90.0±0.4	0.77±0.00	53.8±0.8	61.8±0.3	931.0±44.5
		40-50	86.3±1.7	55.7±0.8	73.1±0.3	0.71±0.00	38.6±0.8	46.9±0.2	588.6±27.8
		50-60	53.6±1.2	40.7±0.8	58.7±0.3	0.63±0.00	26.3±0.8	34.9±0.1	346.9±26.1
		60-70	30.0±0.8	27.9±0.8	45.9±0.2	0.54±0.01	16.2±0.9	25.5±0.1	186.1±26.0
70-80	15.6±0.5	16.6±0.7	33.0±0.2	0.43±0.01	7.7±0.7	17.0±0.1	93.5±27.4		

TABLE I: For the colliding systems Au-Au at $\sqrt{s_{NN}}=7.7, 11.5, 19.6, 27$ and 39 GeV from BES [38] and Au-Au at $\sqrt{s_{NN}}=62.4, 130$ and 200 GeV [34] studied at RHIC by the STAR Collaboration and Pb-Pb at $\sqrt{s_{NN}}=2.76$ and 5.02 TeV investigated by the ALICE Collaboration at LHC [35, 37], are shown: the colliding system, the collision energy, the centrality, the average number of participant nucleons in the collision ($\langle N_{part} \rangle$), the overlapping areas corresponding to the wounded nucleons ($S_{\perp}^{geom}, S_{\perp}^{var}$), estimated by the two recipes explained in the text, the percentage of the wounded nucleons undergoing more than a single collision (f_{core}), the corresponding areas of the wounded nucleons undergoing more than a single collision ($(S_{\perp}^{geom})^{core}, (S_{\perp}^{var})^{core}$) and the hadron density (dN/dy).

The centrality dependent values were rescaled by the factor obtained dividing the geometrical area to S in the

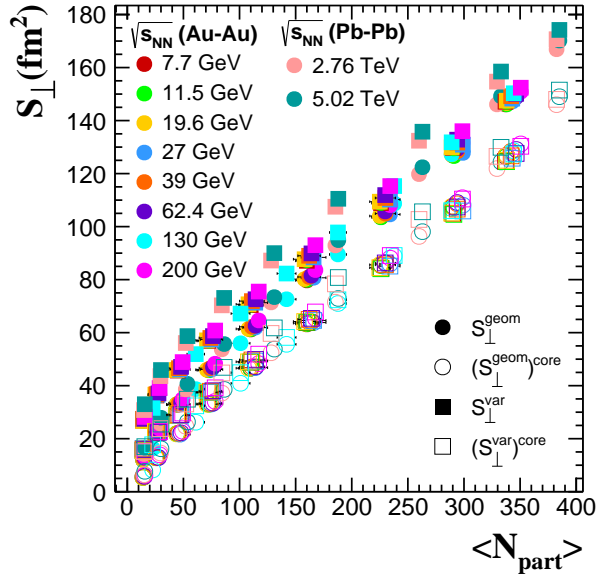


FIG. 1. Overlapping area of the colliding nuclei at different $\sqrt{s_{NN}}$ energies estimated within the GMC approach corresponding to all wounded nucleons S_{\perp}^{geom} (S_{\perp}^{var}) - full dots (full squares) and to the core contribution ($(S_{\perp}^{geom})_{core}$) ($(S_{\perp}^{var})_{core}$) - open dots (open squares) as a function of $\langle N_{part} \rangle$.

case of the complete overlap of the nuclei ($b=0$ fm). The $\langle N_{part} \rangle$ dependence of the overlap area of the colliding nuclei at different energies estimated within the GMC approach corresponding to all wounded nucleons and to the core contribution are presented in Fig.1. $\sqrt{(dN/dy)/S_{\perp}^{geom}}$ as a function of $\sqrt{s_{NN}}$ for different centralities is represented in Fig.2. As an example, in Fig.3 the percentage of the nucleons suffering a single collision as a function of $\langle N_{part} \rangle$ and impact parameter is represented for the lowest and highest $\sqrt{s_{NN}}$ Au-Au collisions, i.e 7.7 and 200 GeV, and for Pb-Pb at the highest LHC energy, $\sqrt{s_{NN}}=5.02$ TeV. As expected, the $\langle N_{part} \rangle$ dependence of the percentage of nucleons undergoing a single collision is less dependent on $\sqrt{s_{NN}}$ than on the impact parameter.

III. dN/dy ESTIMATES

The total hadron density per unit of rapidity has been estimated based on the published identified charged hadrons densities [34, 35, 38, 40] and hyperons densities [42–48]. For $\sqrt{s_{NN}}=19.6$ and 27 GeV BES energies or some of the centralities, where the hyperon yields were not reported, the corresponding values were obtained by interpolation using the energy and centrality dependence fits.

As far as Ω^{-} and $\bar{\Omega}^{+}$ yield values for BES were not reported and the extrapolation from higher energies down

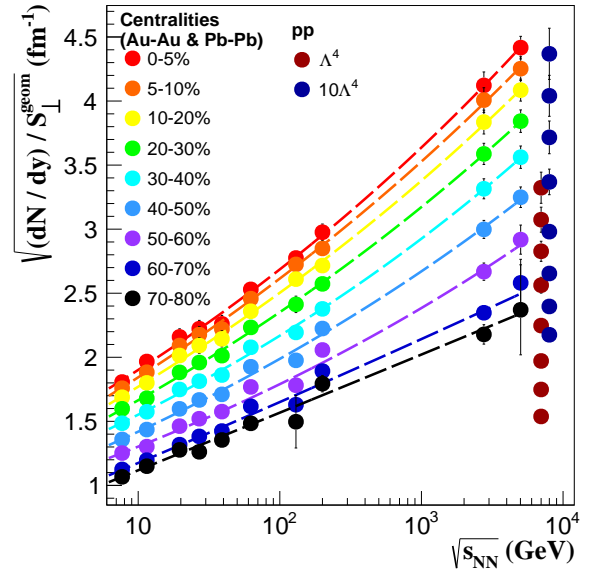


FIG. 2. $\sqrt{(dN/dy)/S_{\perp}^{geom}}$ as a function of $\sqrt{s_{NN}}$ for different centralities based on the values listed in Table I. The dashed lines represent the fit results using a power law function. Dark red and dark blue full dots correspond to pp collision at $\sqrt{s}=7$ TeV, the values being estimated based on the IP-Glasma initial state model, using two values of the α parameter (see Chapter VII). For better clarity, the blue dots were artificially displaced in $\sqrt{s_{NN}}$.

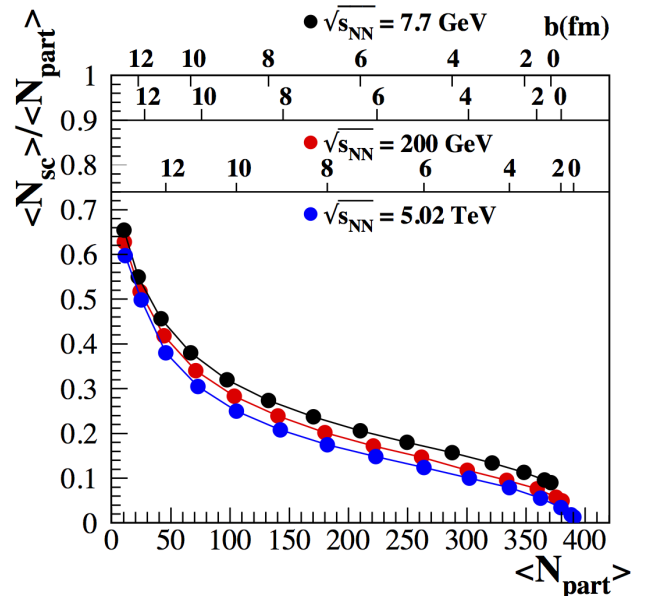


FIG. 3. The percentage of the nucleons suffering a single collision as a function of $\langle N_{part} \rangle$ and impact parameter for Au-Au collisions at $\sqrt{s_{NN}}=7.7$ and 200 GeV and Pb-Pb collisions at $\sqrt{s_{NN}}=5.02$ TeV.

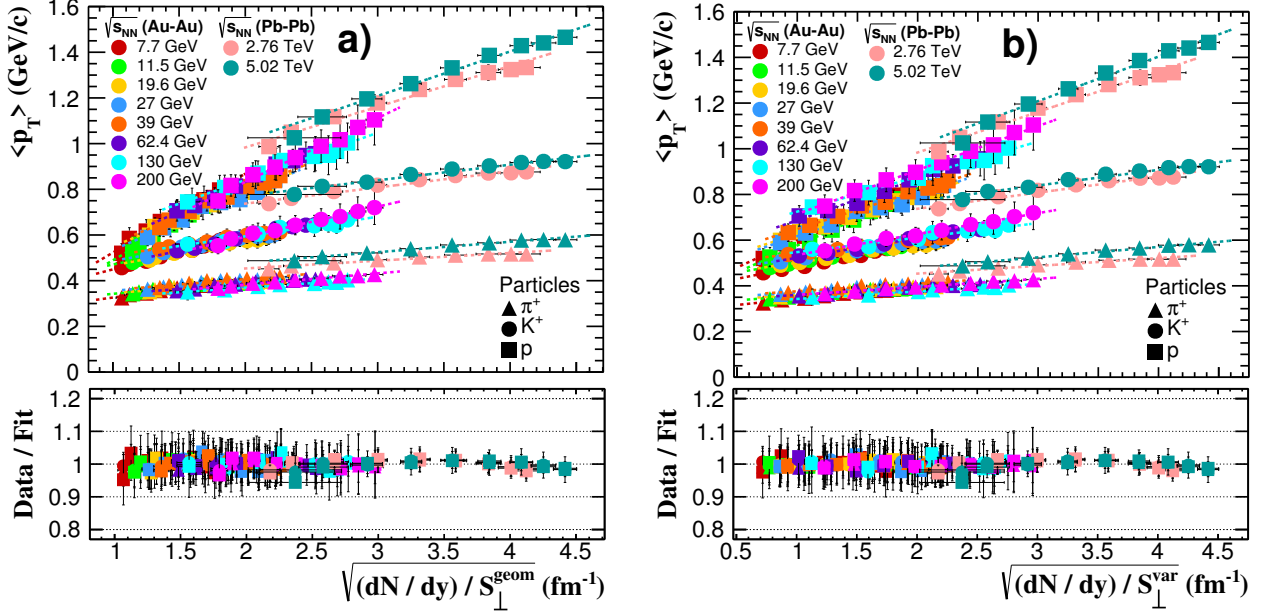


FIG. 4. a) Top: $\langle p_T \rangle$ of pions, kaons and protons for all measured energies and centralities at RHIC and LHC reported by the STAR [34, 38] and ALICE [35, 40] Collaborations, dashed lines representing the results of the first order polynomial fit; bottom: the ratio of the data points to the result of the linear fit for each collision energy, as a function of $\sqrt{\frac{dN}{dy}/S_{\perp}^{geom}}$. b) Same as a) but as a function of $\sqrt{\frac{dN}{dy}/S_{\perp}^{var}}$.

to BES energies shows a negligible contribution, they were not considered in the produced hadron density estimates. Therefore, we used the following approximations: for the BES energies $\frac{dN}{dy} \simeq \frac{3}{2} \frac{dN}{dy}(\pi^+ + \pi^-) + 2 \frac{dN}{dy}(K^+ + K^-, p + \bar{p}, \Xi^- + \bar{\Xi}^+) + \frac{dN}{dy}(\Lambda + \bar{\Lambda})$, from $\sqrt{s_{NN}}=62.4$ GeV to $\sqrt{s_{NN}}=200$ GeV $\frac{dN}{dy} \simeq \frac{3}{2} \frac{dN}{dy}(\pi^+ + \pi^-) + 2 \frac{dN}{dy}(K^+ + K^-, p + \bar{p}, \Xi^- + \bar{\Xi}^+) + \frac{dN}{dy}(\Lambda + \bar{\Lambda}, \Omega^- + \bar{\Omega}^+)$ and for the LHC energies $\frac{dN}{dy} \simeq \frac{3}{2} \frac{dN}{dy}(\pi^+ + \pi^-) + 2 \frac{dN}{dy}(p + \bar{p}, \Xi^- + \bar{\Xi}^+) + \frac{dN}{dy}(K^+ + K^-, K_S^0 + \bar{K}_S^0, \Lambda + \bar{\Lambda}, \Omega^- + \bar{\Omega}^+)$. The values are listed in the last column of Table I.

IV. $\sqrt{\frac{dN}{dy}/S_{\perp}}$ DEPENDENCE OF $\langle p_T \rangle$

As it was already mentioned in the Introduction, in the local parton-hadron duality approach [8], $\langle p_T \rangle / \sqrt{\frac{dN}{dy}/S_{\perp}}$ is proportional with $\frac{1}{n\sqrt{n}}$ where n is the number of charged hadrons produced via gluon fragmentation [9, 10]. Therefore, neglecting other effects like

collective hydrodynamic expansion and suppression, $\langle p_T \rangle / \sqrt{\frac{dN}{dy}/S_{\perp}}$ is expected to decrease in central collisions and at higher energies. $\langle p_T \rangle$ for Au-Au collisions at $\sqrt{s_{NN}}=7.7, 11.5, 19.6, 27, 39$ GeV [38]; $\sqrt{s_{NN}}=62.4, 130, 200$ GeV [34] and Pb-Pb collisions at $\sqrt{s_{NN}}=2.76, 5.02$ TeV [35, 40] for positive pions, kaons and protons are represented as a function of $\sqrt{\frac{dN}{dy}/S_{\perp}}$ in Fig.4a for S_{\perp}^{geom} and in Fig.4b for S_{\perp}^{var} . The data points corresponding to each collision energy were fitted with a first order polynomial function. The trends in the two figures are rather similar and the fit quality, in terms of Data/Fit ratios, presented in the bottom plots of Fig.4 is equally good. The fit parameters are listed in Table II and Table III for $S_{\perp} = S_{\perp}^{geom}$ and $S_{\perp} = S_{\perp}^{var}$, respectively and represented in Fig.5.

The slope value increases from pions to protons. Although the experimental error bars are rather large at the RHIC energies, a systematic decrease of the slopes with the collision energy is evidenced for the $\langle p_T \rangle$ dependence on $\sqrt{\frac{dN}{dy}/S_{\perp}^{geom}}$ - full symbols. This trend is enhanced going from pions to protons. The offset values are rather similar at the RHIC energies and increase for

$\sqrt{s_{NN}}$ (GeV)	Slope			Offset		
	π^+	K^+	p	π^+	K^+	p
7.7	0.08 ± 0.02	0.15 ± 0.03	0.35 ± 0.07	0.25 ± 0.03	0.30 ± 0.04	0.18 ± 0.10
11.5	0.05 ± 0.02	0.12 ± 0.03	0.33 ± 0.07	0.29 ± 0.04	0.35 ± 0.05	0.16 ± 0.10
19.6	0.05 ± 0.02	0.11 ± 0.04	0.24 ± 0.05	0.30 ± 0.04	0.36 ± 0.06	0.31 ± 0.08
27	0.05 ± 0.02	0.10 ± 0.03	0.25 ± 0.05	0.31 ± 0.04	0.39 ± 0.06	0.29 ± 0.08
39	0.05 ± 0.02	0.08 ± 0.04	0.24 ± 0.05	0.31 ± 0.05	0.43 ± 0.07	0.33 ± 0.09
62.4	0.05 ± 0.01	0.12 ± 0.02	0.26 ± 0.05	0.30 ± 0.03	0.35 ± 0.04	0.31 ± 0.09
130	0.04 ± 0.02	0.09 ± 0.02	0.21 ± 0.05	0.29 ± 0.04	0.42 ± 0.05	0.43 ± 0.10
200	0.05 ± 0.02	0.13 ± 0.04	0.28 ± 0.06	0.28 ± 0.04	0.33 ± 0.09	0.27 ± 0.13
2760	0.03 ± 0.01	0.07 ± 0.01	0.18 ± 0.02	0.39 ± 0.03	0.60 ± 0.05	0.63 ± 0.05
5020	0.05 ± 0.01	0.07 ± 0.01	0.19 ± 0.02	0.39 ± 0.04	0.64 ± 0.04	0.63 ± 0.06

TABLE II. The parameters for the linear fit of the $\langle p_T \rangle$ dependence on $\sqrt{\frac{dN}{dy}}/S_{\perp}^{geom}$ for pions, kaons and protons corresponding to the energies mentioned in the first column.

$\sqrt{s_{NN}}$ (GeV)	Slope			Offset		
	π^+	K^+	p	π^+	K^+	p
7.7	0.05 ± 0.02	0.11 ± 0.02	0.24 ± 0.05	0.29 ± 0.02	0.38 ± 0.03	0.36 ± 0.06
11.5	0.04 ± 0.02	0.09 ± 0.02	0.24 ± 0.04	0.32 ± 0.02	0.42 ± 0.03	0.34 ± 0.06
19.6	0.04 ± 0.02	0.08 ± 0.02	0.17 ± 0.03	0.33 ± 0.03	0.42 ± 0.04	0.46 ± 0.05
27	0.03 ± 0.02	0.07 ± 0.02	0.18 ± 0.03	0.34 ± 0.03	0.45 ± 0.04	0.44 ± 0.05
39	0.03 ± 0.02	0.06 ± 0.03	0.17 ± 0.03	0.34 ± 0.03	0.48 ± 0.04	0.48 ± 0.05
62.4	0.03 ± 0.01	0.09 ± 0.02	0.18 ± 0.03	0.33 ± 0.02	0.44 ± 0.03	0.51 ± 0.06
130	0.03 ± 0.01	0.06 ± 0.02	0.15 ± 0.03	0.31 ± 0.03	0.48 ± 0.04	0.57 ± 0.06
200	0.04 ± 0.01	0.09 ± 0.03	0.19 ± 0.04	0.33 ± 0.03	0.44 ± 0.05	0.52 ± 0.08
2760	0.03 ± 0.01	0.07 ± 0.01	0.18 ± 0.02	0.39 ± 0.03	0.60 ± 0.04	0.63 ± 0.05
5020	0.05 ± 0.01	0.07 ± 0.01	0.19 ± 0.02	0.39 ± 0.04	0.64 ± 0.04	0.62 ± 0.06

TABLE III. The parameters for the linear fit of the $\langle p_T \rangle$ dependence on $\sqrt{\frac{dN}{dy}}/S_{\perp}^{var}$ for pions, kaons and protons corresponding to the energies mentioned in the first column.

all the three species at LHC energies. Using S_{\perp}^{var} , Fig.4b, the extracted slopes, represented in Fig.5a by open symbols show a marginal variation as a function of collision energy - dashed lines. The corresponding offsets, represented in Fig.5b by open symbols, within the error bars, are the same for pions and kaons and are systematically larger for protons at RHIC energies compared with the ones corresponding to S_{\perp}^{geom} . One should remark that at LHC energies, the results using S_{\perp}^{geom} or S_{\perp}^{var} are the same. At the LHC energies, in the most central collisions, a saturation trend seems to develop. A natural question which comes is how much of the observed trends is due to core-corona interplay [49–56] and how the $\langle p_T \rangle$ - $\sqrt{\frac{dN}{dy}}/S_{\perp}$ correlation for core looks like. Based on the recipe presented in [56], we estimated the $\langle p_T \rangle^{core}$ for pions, kaons and protons for $\sqrt{s_{NN}}=200$ GeV, 2.76 TeV and 5.02 TeV:

$$\langle p_T \rangle_i^{cen} = \frac{f_{core} \langle p_T \rangle_i^{core} M_i^{core} + (1 - f_{core}) \langle p_T \rangle_i^{ppMB} M_i^{ppMB}}{f_{core} M_i^{core} + (1 - f_{core}) M_i^{ppMB}} \quad (2)$$

$\langle p_T \rangle_i^{ppMB}$ for π^+ , K^+ , p in pp minimum bias (MB) collisions at $\sqrt{s_{NN}}=200$ GeV were reported by the STAR Collaboration [34] and at $\sqrt{s_{NN}}=2.76$ TeV and 5.02

TeV were reported by the ALICE Collaboration [57, 58]. $(dN/dy)^{core}$ at the same energies were estimated using:

$$\left(\frac{dN}{dy} \right)_i^{cen} = \langle N_{part} \rangle [(1 - f_{core}) M_i^{ppMB} + f_{core} M_i^{core}] \quad (3)$$

where $M_i^{ppMB} = \frac{1}{2} (dN/dy)_i^{ppMB}$ at the same energy and M_i^{core} is the multiplicity per core participant. $(dN/dy)_i^{ppMB}$ for π^+ , K^+ , p were obtained based on the MB p_T spectra reported in [57, 58].

In Fig.6a $\langle p_T \rangle$ as a function of $\sqrt{\frac{dN}{dy}}/S_{\perp}^{geom}$ for pions, kaons and protons for $\sqrt{s_{NN}}=200$ GeV, 2.76 TeV and 5.02 TeV is represented. The experimental points for each energy and each species were fitted with linear functions. As it was already mentioned above, at $\sqrt{s_{NN}}=2.76$ TeV and 5.02 TeV the very last three points, corresponding to the most central collisions, systematically deviate from a linear trend observed at lower centralities and therefore were excluded from the fit. The slopes and the offsets are presented in Table IV. The fit quality can be followed in the bottom plot of Fig.6a where the ratios between the data points and fit results are represented. One can also observe that the last three points at $\sqrt{s_{NN}}=2.76$ TeV and 5.02 TeV, corresponding

$\sqrt{s_{NN}}$ (GeV)	Slope			Offset		
	π^+	K^+	p	π^+	K^+	p
200	0.05 ± 0.02	0.13 ± 0.04	0.28 ± 0.06	0.28 ± 0.04	0.33 ± 0.09	0.27 ± 0.13
2760	0.04 ± 0.01	0.09 ± 0.02	0.20 ± 0.03	0.37 ± 0.04	0.56 ± 0.07	0.56 ± 0.08
5020	0.05 ± 0.02	0.08 ± 0.02	0.22 ± 0.03	0.37 ± 0.06	0.60 ± 0.07	0.54 ± 0.10

TABLE IV. The parameters of the linear fit of $\langle p_T \rangle$ as a function of $\sqrt{(\frac{dN}{dy})/S_{\perp}^{geom}}$ for pions, kaons and protons corresponding to $\sqrt{s_{NN}}=200$ GeV, 2.76 TeV and 5.02 TeV collision energies. The very last three points at $\sqrt{s_{NN}}=2.76$ and 5.02 TeV were not included in the fit.

$\sqrt{s_{NN}}$ (GeV)	Slope			Offset		
	π^+	K^+	p	π^+	K^+	p
200	0.02 ± 0.03	0.09 ± 0.06	0.20 ± 0.11	0.36 ± 0.07	0.43 ± 0.15	0.50 ± 0.29
2760	0.03 ± 0.02	0.07 ± 0.03	0.17 ± 0.04	0.40 ± 0.06	0.58 ± 0.10	0.66 ± 0.14
5020	0.03 ± 0.03	0.06 ± 0.02	0.17 ± 0.04	0.41 ± 0.11	0.65 ± 0.08	0.73 ± 0.16

TABLE V. The parameters of the linear fit of $\langle p_T \rangle$ as a function of $\sqrt{(\frac{dN}{dy})^{core}/S_{\perp}^{core}}$ for pions, kaons and protons corresponding to $\sqrt{s_{NN}}=200$ GeV, 2.76 TeV and 5.02 TeV collision energies. For $\sqrt{s_{NN}}=2.76$ TeV and 5.02 TeV, the last three centralities, where a levelling off is evidenced, were not included in the fit.

to the most central collisions, deviate from the general trend, the ratio $\langle p_T \rangle / \sqrt{\frac{dN}{dy}/S_{\perp}}$ is decreasing, as expected in Ref.[10].

For $\sqrt{s_{NN}}=200$ GeV, 2.76 TeV and 5.02 TeV we estimated $\langle p_T \rangle^{core}$ and $\sqrt{\frac{dN}{dy}^{core}/(S_{\perp}^{geom})^{core}}$, the results being presented in Fig.6b.

The quality of the linear fit, represented in the bottom plot of Fig.6b is equally good as for the experimental data but the slope values presented in Table V are systematically smaller and the difference between the highest RHIC energy and the LHC energies is reduced. The saturation towards the most central collisions at LHC energies does not change.

V. $\langle p_T \rangle$ PARTICLE MASS DEPENDENCE AS A FUNCTION OF $\sqrt{\frac{dN}{dy}/S_{\perp}^{geom}}$

The $\langle p_T \rangle$ dependence on the mass of pions, kaons and protons at different collision centralities, except for the most peripheral ones, is linear. Therefore, linear fits of the $\langle p_T \rangle$ particle mass dependence, corresponding to each centrality and energy considered in the paper, were performed. The extracted fit parameters as a function of $\sqrt{\frac{dN}{dy}/S_{\perp}^{geom}}$ are shown in Fig.7 (slope) and Fig.8 (offset). In Fig.7 the slopes are fitted with the following expression:

$$Slope_{\langle p_T \rangle=f(mass)} = \alpha + \beta \left(\sqrt{\frac{dN}{dy}/S_{\perp}^{geom}} \right)^{\gamma} \quad (4)$$

The slopes for particles Fig.7a and antiparticles Fig.7b evidence a $\sqrt{\frac{dN}{dy}/S_{\perp}^{geom}}$ dependence which closely follows a trend given by Eq.4 (dashed lines). The val-

ues of the fit parameters are listed in Fig.7. The fit quality is represented in the bottom plots of Fig.7a and Fig.7b in terms of Data/Fit. Besides the points corresponding to the most central collisions at $\sqrt{s_{NN}}=19.6$, 27 and 39 GeV which deviate from the fit by $\sim 10-15\%$, the bulk of data nicely cluster around the fit curve, well within the error bars. In Fig.8, although the error bars are rather large, a systematic increase of the offsets as a function of $\sqrt{\frac{dN}{dy}/S_{\perp}^{geom}}$ is evidenced at BES energies and at $\sqrt{s_{NN}}=62.4$ GeV, reaching a plateau above $1.7 fm^{-1}$. This trend is much reduced starting from $\sqrt{s_{NN}}=130$ GeV. Therefore, we considered only offsets above $1.7 fm^{-1}$ and found their average values for different $\sqrt{s_{NN}}$. The results are presented in Fig.9.

VI. $\sqrt{\frac{dN}{dy}/S_{\perp}^{geom}}$ DEPENDENCE OF BOLTZMANN-GIBBS BLAST WAVE FIT PARAMETERS

The p_T spectra for identified charged hadrons were fitted [34, 35, 38, 40, 41] using the BGBW expression inspired by hydrodynamic models [59]:

$$E \frac{d^3N}{dp^3} \sim \int_0^R m_T K_1(m_T \cosh \rho / T_{kin}^{fo}) I_0(p_T \sinh \rho / T_{kin}^{fo}) r dr \quad (5)$$

where $m_T = \sqrt{m^2 + p_T^2}$; $\beta_T(r) = \beta_s(\frac{r}{R})^n$; $\rho = \tanh^{-1} \beta_T$. T_{kin}^{fo} is the kinetic freeze-out temperature and n defines the expansion profile. A compilation of all results in terms of the $\langle p_T \rangle$ dependence on $\sqrt{\frac{dN}{dy}/S_{\perp}^{geom}}$ is presented in Fig.10. One should mention that for the BES energies [38] the BGBW fits were performed simultaneously on particles and antiparticles p_T spectra, although they do not present the same trends in many

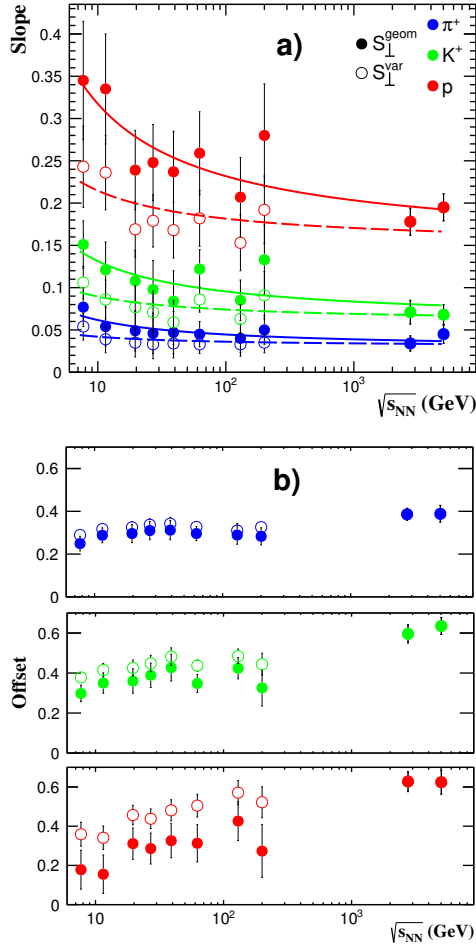


FIG. 5. a) The slopes of the $\langle p_T \rangle$ dependence on $\sqrt{\frac{dN}{dy}/S_{\perp}^{geom}}$ (full symbols) and on $\sqrt{\frac{dN}{dy}/S_{\perp}^{var}}$ (open symbols) for π^+ (blue), K^+ (green) and p (red) as a function of $\sqrt{s_{NN}}$. The fit results with the function $a+b/(\log\sqrt{s_{NN}})$ are drawn with full (S_{\perp}^{geom}) and dashed (S_{\perp}^{var}) lines. b) The corresponding offsets.

respects. Therefore, in Fig.10, the $\langle\beta_T\rangle$ for antiparticles for some energies and centralities, where the azimuthal dependent BGBW fits were published [60, 61], were represented by open symbols. One could observe that, with increasing collision energy, the values of $\langle\beta_T\rangle$ for antiparticles converge towards the values obtained from a simultaneous fit of particles and antiparticles p_T spectra [34, 38]. However, the $\langle\beta_T\rangle$ values reported in the literature, scale rather nice as a function of $\sqrt{\frac{dN}{dy}/S_{\perp}^{geom}}$ and a 4th order polynomial function fits them well. The fit quality can be followed in the bottom plot of Fig.10. Within the experimental error bars, all data follow the fit result, except the points corresponding to the peripheral collisions at the lowest BES energies. The fit parameters are included in the figure. The same representation in

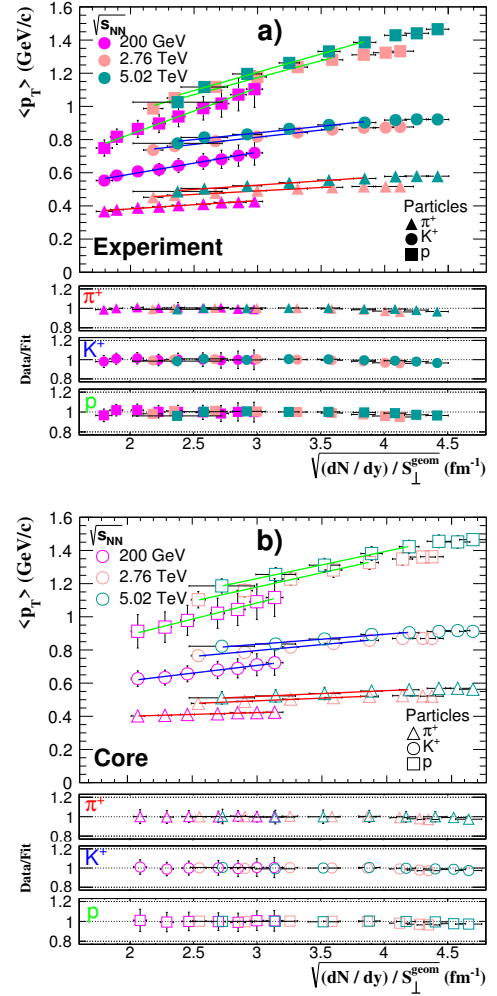


FIG. 6. $\langle p_T \rangle$ as a function of $\sqrt{\frac{dN}{dy}/S_{\perp}^{geom}}$ for identified charged hadrons for $\sqrt{s_{NN}}=200$ GeV, 2.76 TeV and 5.02 TeV. The full lines represent the results of the first order polynomial fit. a) Top: experimental results; Bottom: Data/Fit ratio; b) Top: estimated core contribution; Bottom: Data/Fit ratio.

which the data corresponding to $\sqrt{s_{NN}}=7.7, 11.5$ and 62.4 GeV are excluded, can be followed in Fig.11. For the remaining energies, from $\sqrt{s_{NN}}=19.6$ GeV to 5.02 TeV a much better scaling is observed. The dynamics in $\langle\beta_T\rangle$ as a function of $\sqrt{\frac{dN}{dy}/S_{\perp}^{geom}}$ for different collision energies can be easier followed in Fig.12 where the ratio between $\langle\beta_T\rangle$ at a given centrality relative to $\langle\beta_T\rangle$ in the most peripheral collisions, $70\%-80\%$ ($58\%-85\%$ for 130 GeV), $\langle\beta_T\rangle/\langle\beta_T^{Peripheral}\rangle$, is plotted as a function of $\sqrt{\frac{dN}{dy}/S_{\perp}^{geom}}$ for all energies.

In Fig.13 the T_{kin}^{fo} and n parameters and their dependence on $\sqrt{\frac{dN}{dy}/S_{\perp}^{geom}}$ are presented. A close to linear dependence with a negative slope is observed in Fig.13a, for T_{kin}^{fo} at RHIC energies. Within the error bars, it is rather difficult to conclude on some collision energy de-

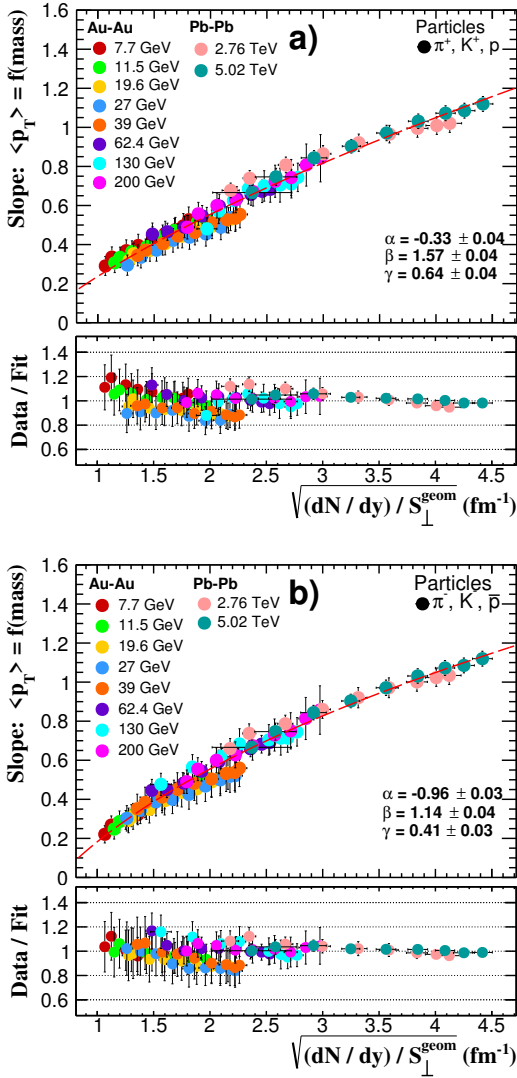


FIG. 7. The slopes from the linear fit of $\langle p_T \rangle$ versus particle mass as a function of $\sqrt{\frac{dN}{dy}/S_{\perp}^{\text{geom}}}$, for each centrality and energy, for a) π^+ , K^+ , p and b) π^- , K^- , \bar{p} . The continuous red line is the result of the fit with the function from Eq.4. The ratios Data/Fit are represented in the bottom plots of each of the two figures.

pendence of T_{kin}^{fo} for a given value of the geometrical variable. On the other hand, a significant shift of about 20 MeV in T_{kin}^{fo} fit parameter towards larger values is evidenced for a given $\sqrt{\frac{dN}{dy}/S_{\perp}^{\text{geom}}}$ at LHC energies relative to the RHIC energies. Similar shifts were mentioned in the previous chapters for $\langle p_T \rangle$ and the offsets of $\langle p_T \rangle$ as a function of mass. Such a shift is also evidenced in the T_{kin}^{fo} versus $\langle \beta_T \rangle$ representation in Fig.14 where the fit parameters reported in Ref. [34, 35, 38, 40, 41] are used. As far as the n dependence on $\sqrt{\frac{dN}{dy}/S_{\perp}^{\text{geom}}}$ is concerned, Fig.13b, the values for BES energies are rather scattered and those corresponding to 62.4 and 200 GeV show an

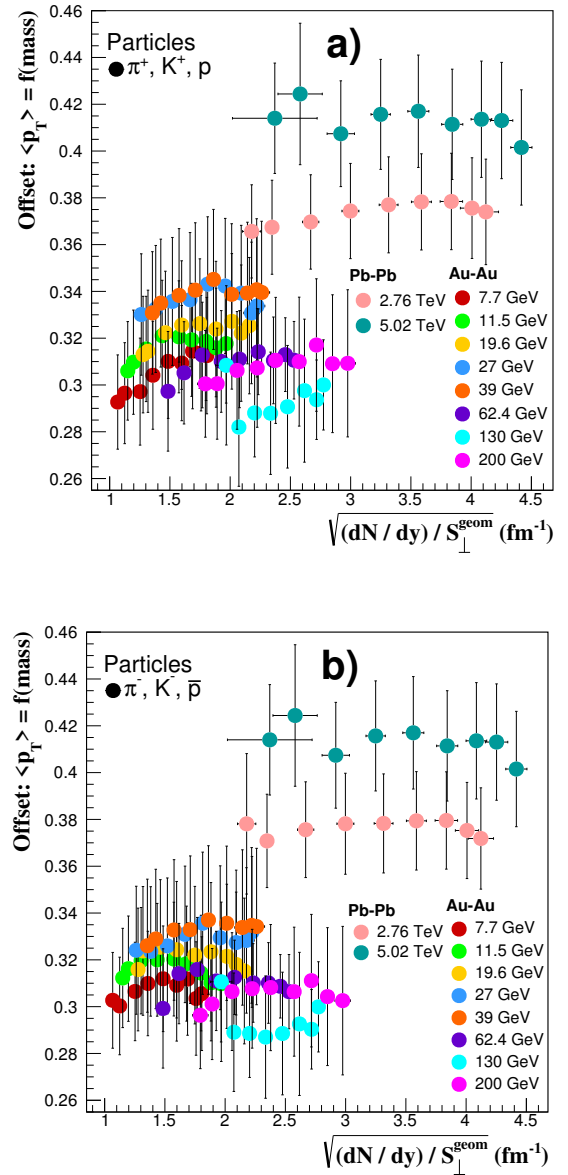


FIG. 8. The offsets from the linear fits of $\langle p_T \rangle$ versus particle mass dependence as a function of $\sqrt{\frac{dN}{dy}/S_{\perp}^{\text{geom}}}$; a) particles, b) antiparticles.

opposite trend to what is observed at LHC. Usually, the flow profile changes from a shell type expansion, large n values, towards $n=1$ (Hubble type) with increasing centrality, even smaller than 1 for very central collisions. It is worth mentioning that for a consistent interpretation, the fits of the p_T spectra using the BGBW expression have to be done at all energies on the same p_T range for a given species. The range has to be chosen such to reduce as much as possible the influence of processes other than collective expansion on the extracted fit parameters. Therefore, the lower limit of the fit range for pions has to be chosen such that the contribution coming from resonance decays is reduced, while the upper fit ranges for

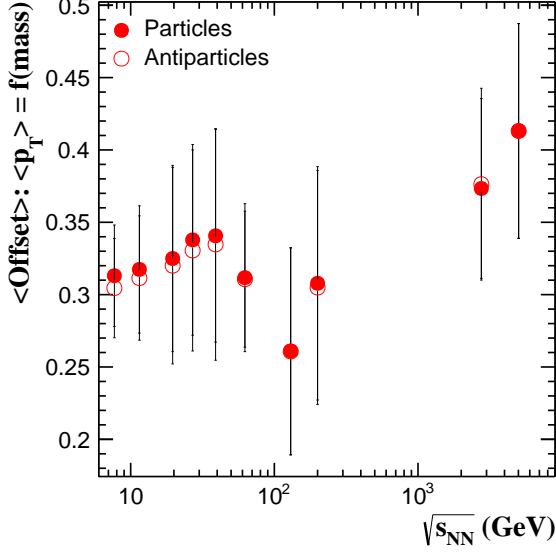


FIG. 9. The average values of the offsets of the $\langle p_T \rangle$ mass dependence for $\sqrt{\frac{dN}{dy}/S_{\perp}^{geom}} \geq 1.7 \text{ fm}^{-1}$ as a function of $\sqrt{s_{NN}}$. Full symbols - particles; open symbols - antiparticles.

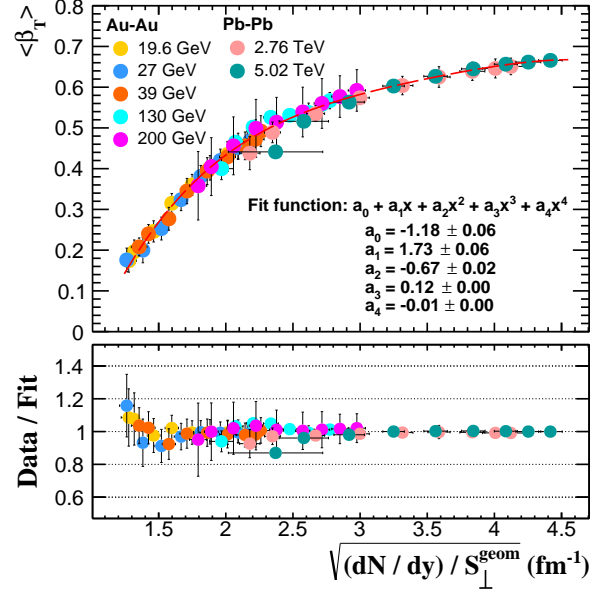


FIG. 11. The BGBW fit parameter $\langle \beta_T \rangle$ as a function of $\sqrt{\frac{dN}{dy}/S_{\perp}^{geom}}$ excluding $\sqrt{s_{NN}}=7.7, 11.5$ and 62.4 GeV collision energies.

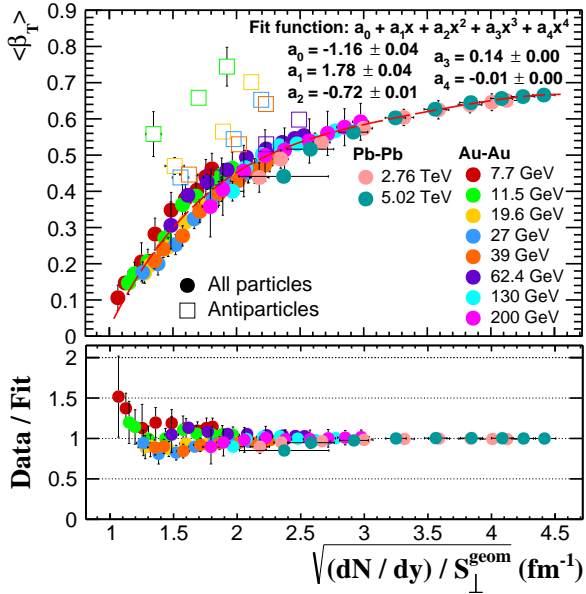


FIG. 10. Top: the BGBW fit parameter $\langle \beta_T \rangle$ as a function of $\sqrt{\frac{dN}{dy}/S_{\perp}^{geom}}$, the dashed red line corresponds to the result of the fit using a 4th order polynomial function. Bottom: the Data/Fit ratio.

all species have to be optimised in order to be influenced as little as possible by the suppression effects. Last but not least, the influence of the corona contribution on the fit parameters has to be carefully considered.

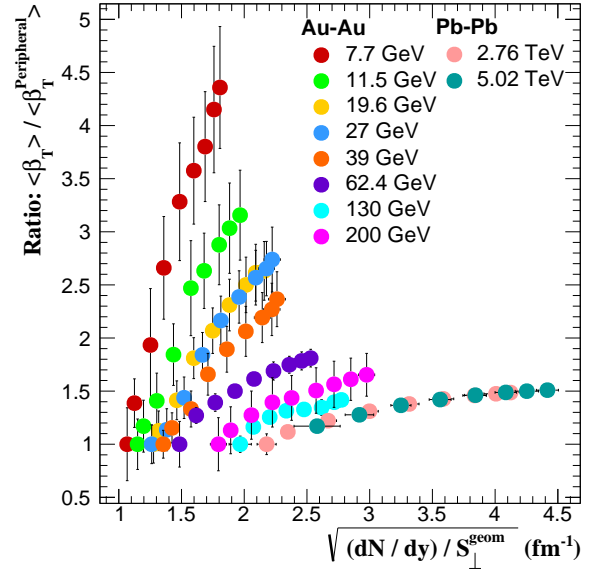


FIG. 12. $\langle \beta_T \rangle / \langle \beta_T^{Peripheral} \rangle$ as a function of $\sqrt{\frac{dN}{dy}/S_{\perp}^{geom}}$. $\langle \beta_T \rangle$ fit parameters were reported in Ref. [34, 35, 38, 40].

VII. COMPARISON BETWEEN pp AND $Pb - Pb$ SYSTEMS AT LHC ENERGIES

Similarities between pp and $Pb - Pb$ in terms of the behaviour of different observables, like the $(\langle \beta_T \rangle - T_{kin}^{fo})$

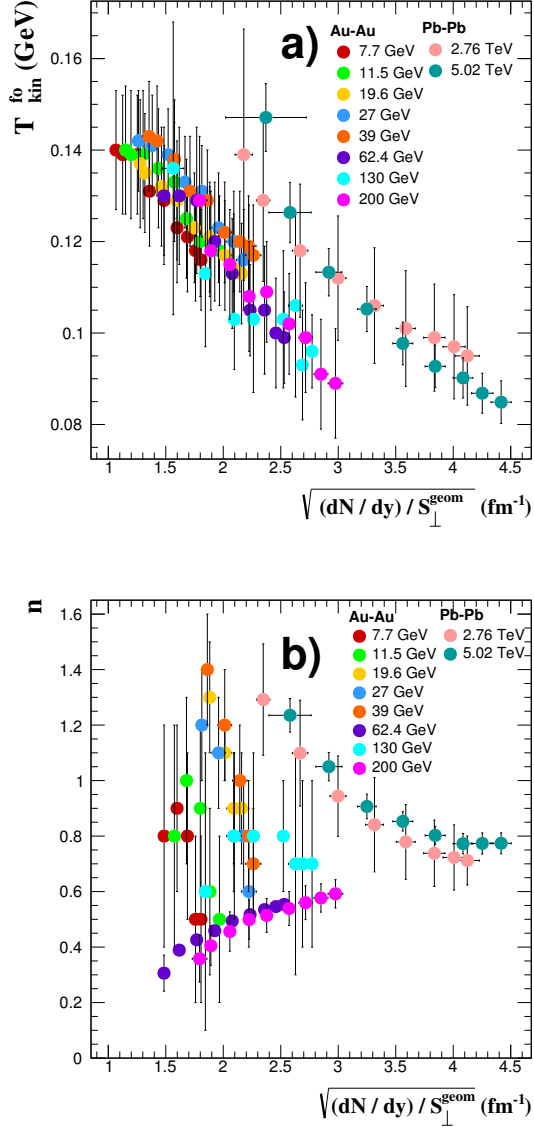


FIG. 13. a) T_{kin}^{fo} and b) n parameters as a function of $\sqrt{\frac{dN}{dy}/S_{\perp}^{geom}}$. The fit parameters were taken from [34, 35, 38, 40, 41].

correlation as a function of charged particle multiplicity [15] and near-side long range pseudorapidity correlations at large charged particle multiplicities [11], were evidenced at LHC energies. The extent to which the similarity between pp and Pb-Pb is also evidenced in the behaviour of the observables described in the previous chapters as a function of the saturation momentum, i.e. $\sqrt{\frac{dN}{dy}/S_{\perp}}$, is further investigated. For this comparison we used the results of the ALICE Collaboration for p_T spectra of identified light flavour charged hadrons as a function of charged particle multiplicity at mid-rapidity as well as the results of their fits with the BGBW expression given by Eq.5 [15]. The hadron density per unit of

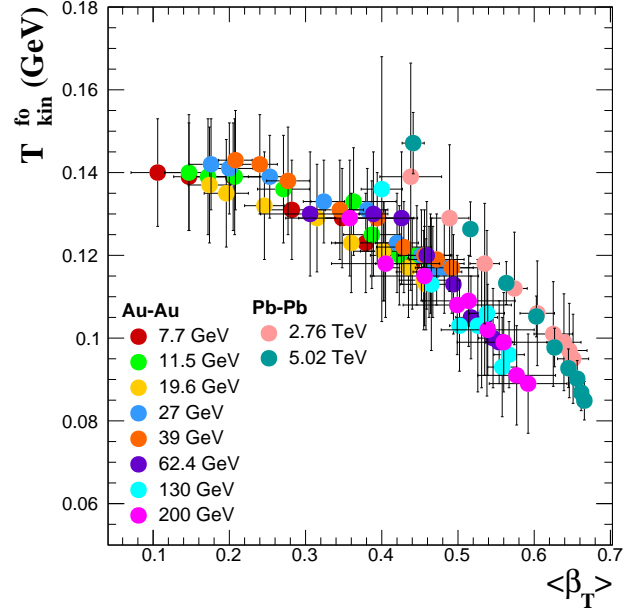


FIG. 14. The BGBW fit parameters T_{kin}^{fo} versus $\langle\beta_T\rangle$ reported in [34, 35, 38, 40, 41].

rapidity for the mid-central charged particle multiplicity was estimated by extrapolating the results reported by the ALICE Collaboration in Ref. [17]. The $\langle p_T \rangle$ values were estimated based on the p_T spectra from [15] extrapolated in the unmeasured regions using fits of the measured spectra with the expression from [62]:

$$\frac{d\sigma}{p_T dp_T} = A_e \exp(-E_T^{kin}/T_e) + \frac{A}{\left(1 + \frac{p_T^2}{T^2 \cdot n}\right)^n} \quad (6)$$

The interaction area for pp collisions, $S_{\perp}^{pp} = \pi R_{pp}^2$, is calculated using the estimates of the maximal radius for which the energy density of the Yang-Mill fields is larger than $\varepsilon = \alpha \Lambda_{QCD}^4$ ($\alpha \in [1, 10]$) within the IP-Glasma initial state model [63, 64]. Within the present knowledge of QCD, α cannot be precisely estimated. The r_{max} values used in Ref. [63] for $\alpha=1$ were fitted in Ref. [65] with the following expressions:

$$f_{pp} = \begin{cases} 0.387 + 0.0335x + 0.274x^2 - 0.0542x^3 & \text{if } x < 3.4 \\ 1.538 & \text{if } x \geq 3.4 \end{cases} \quad (7)$$

Using the same recipe we fitted the r_{max} values from Ref. [63] for $\alpha=10$ with the following expression:

$$f_{pp} = \begin{cases} -0.018 + 0.3976x + 0.095x^2 - 0.028x^3 & \text{if } x < 3.4 \\ 1.17 & \text{if } x \geq 3.4 \end{cases} \quad (8)$$

where $x = (dN_g/dy)^{1/3}$. The hadron density per unit of rapidity, estimated based on the following approximation: $\frac{dN}{dy} \simeq \frac{3}{2} \frac{dN}{dy} (\pi^+ + \pi^-) + 2 \frac{dN}{dy} (p + \bar{p}, \Xi^- + \bar{\Xi}^+, K_S^0) +$

\sqrt{s} (TeV) (pp)	dN/dy	S_{\perp} (fm ²)	
		$\alpha = 1$	$\alpha = 10$
7	82.1±2.8	7.43±0.48	4.30±0.36
	70.2±2.2	7.43±0.41	4.30±0.31
	59.4±1.7	7.43±0.35	4.30±0.27
	48.8±1.3	7.43±0.30	4.30±0.23
	37.3±0.9	7.39±0.02	4.20±0.02
	26.8±0.6	6.89±0.05	3.80±0.03
	18.2±0.4	5.94±0.06	3.16±0.04
	10.8±0.2	4.58±0.06	2.29±0.04

TABLE VI. The hadron density per unit of rapidity and transverse overlapping areas for $\alpha=1$ and $\alpha=10$ for pp collisions at $\sqrt{s}=7$ TeV.

$\frac{dN}{dy}(K^+ + K^-, \Lambda + \bar{\Lambda}, \Omega^- + \bar{\Omega}^+)$ and the corresponding overlapping areas for $\alpha=1$ and $\alpha=10$ values are listed in Table VI. The gluon density per unit of rapidity was approximated by $dN_g/dy \approx dN/dy$. The comparison between the $\langle p_T \rangle$ dependence on the square root of the hadron density per unit of rapidity and unit of interaction area for the pp at $\sqrt{s}=7$ TeV and Pb-Pb at $\sqrt{s_{NN}}=2.76$ and 5.02 TeV collisions, based on the results obtained by the ALICE Collaboration [15, 35, 40, 41], is presented in Fig.15. As one could see, the general trend for all the three species is very similar in pp and Pb-Pb collisions. The differences could have several origins, i.e. the difference in the collision energies, a systematic larger $\langle p_T \rangle$

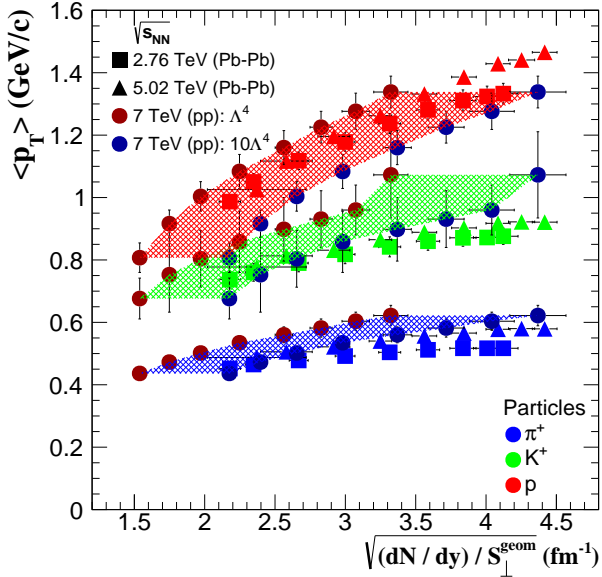


FIG. 15. $\langle p_T \rangle$ for identified charged hadrons for pp collisions at $\sqrt{s}=7$ TeV [15] (dark red symbols - $\alpha=1$, dark blue symbols - $\alpha=10$) and Pb-Pb collisions at $\sqrt{s_{NN}}=2.76$ and 5.02 TeV [35, 40] The blue, green and red shaded areas represent the uncertainty in the overlapping surface estimates for pp collisions, see the text.

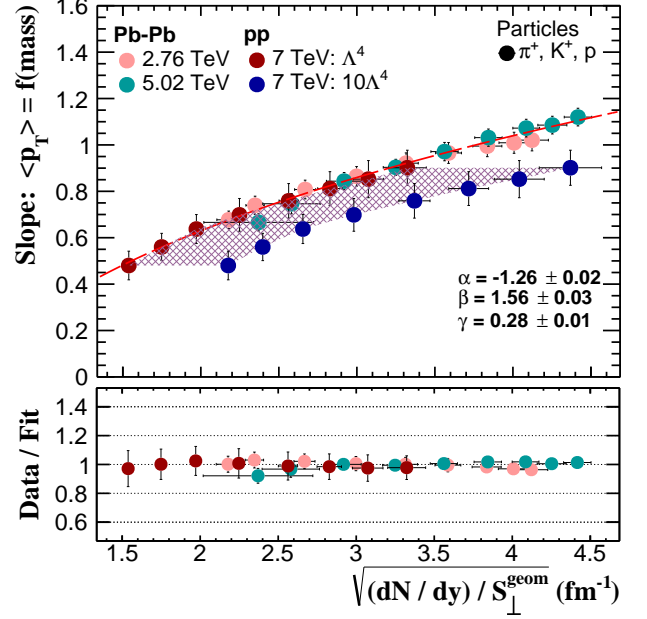


FIG. 16. The slopes of the $\langle p_T \rangle$ particle mass dependence as a function of $\sqrt{\frac{dN}{dy}/S_{\perp}^{geom}}$ for pp at $\sqrt{s}=7$ TeV (red symbols - $\alpha=1$, blue symbols - $\alpha=10$) and Pb-Pb at $\sqrt{s_{NN}}=2.76$ and 5.02 TeV.

for kaons in pp relative to Pb-Pb, uncertainty in estimating the value of α , the large inhomogeneity of the initial state with a direct consequence on the S_{\perp} estimate and last but not least the build up of collective expansion in the hadronic phase and suppression effects taking place in the Pb-Pb case and not yet evidenced in pp collisions. The comparison between the two systems in terms of the slopes of the $\langle p_T \rangle$ particle mass dependence as a function of $\sqrt{\frac{dN}{dy}/S_{\perp}^{geom}}$ is presented in Fig.16. A very good scaling is found using $\alpha=1$ for pp collisions. The same value of α was used in Refs.[65, 66]. These results seem to support the assumption that the global properties of the hadron production are determined by the properties of flux tubes of $\sim 1/\sqrt{\frac{dN}{dy}/S_{\perp}}$ size and are very little influenced by the size of the colliding system [18, 65, 67]. A similar behaviour was evidenced at the baryonic level at much lower energies where the main features of the dynamic evolution of the fireball are determined by the initial baryon density profile and temperature and not too much by its size [68]. As it is well known, the LPHD approach neglects all collective effects. However, a comparison between pp and Pb-Pb collisions in terms of $\langle \beta_T \rangle$, one of the BGBW fit parameters interpreted as the average transverse flow velocity, could be rather interesting. $\langle \beta_T \rangle$ values for pp at $\sqrt{s}=7$ TeV [15] and Pb-Pb at $\sqrt{s_{NN}}=2.76$ and 5.02 TeV [35, 40, 41] reported by the ALICE Collaboration are represented as a function of $\sqrt{\frac{dN}{dy}/S_{\perp}^{geom}}$ in Fig.17. A 4rd degree polynomial func-

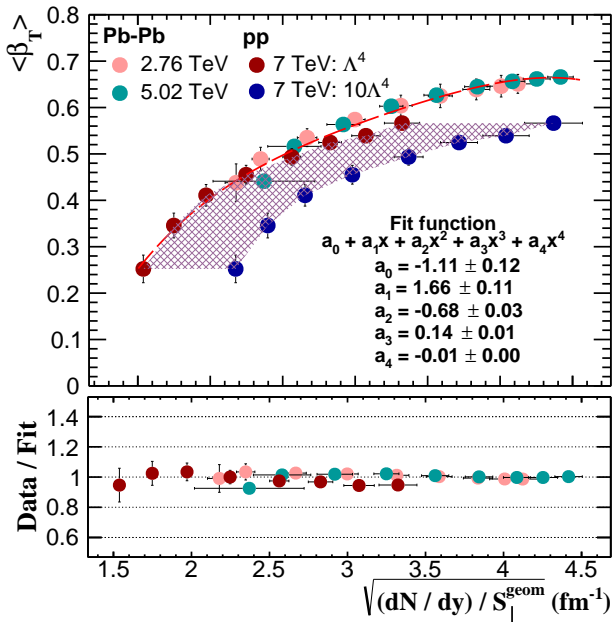


FIG. 17. The BGBW fit parameters $\langle\beta_T\rangle$ as a function of $\sqrt{\frac{dN}{dy}/S_{\perp}^{geom}}$ for pp at $\sqrt{s}=7$ TeV and Pb-Pb at $\sqrt{s_{NN}}=2.76$ and 5.02 TeV. The shaded area represents the uncertainty in the overlapping area estimates for pp collisions, see the text.

tion fits rather well the data corresponding to pp at $\sqrt{s}=7$ TeV ($\alpha=1$) and Pb-Pb at $\sqrt{s_{NN}}=2.76$ and 5.02 TeV. The fit quality is represented in the bottom plot of the figure. Qualitatively the trends are similar and there is even a very good quantitative scaling for $\alpha=1$ used in the estimate of S_{\perp} for the pp case. The origin of the remaining differences was discussed above. This similarity shows that the main features of the dynamical evolution of the systems produced in pp or Pb-Pb collisions at LHC energies are determined by the density of produced hadrons per unit of rapidity and overlapping area.

VIII. CONCLUSIONS

Based on the data for the highest three energies measured at RHIC ($\sqrt{s_{NN}}=62.4, 130, 200$ GeV), the most recent results from BES at RHIC ($\sqrt{s_{NN}}=7.7-39$ GeV) and the highest collision energies at LHC ($\sqrt{s_{NN}}=2.76,$

5.02 TeV), we performed a systematic study of the dependence of different observables on the geometrical variable calculated as the square root of the hadron density per unit of rapidity and unit of overlapping area of two colliding ions. The overlapping area has been estimated in the Glauber MC approach. The experimental $\langle p_T \rangle$ values follow a rather good scaling as a function of this variable for each energy. Linear fits of the experimental data show slopes which increase from pions to protons and decrease from BES to LHC energies. A saturation trend for the most central collisions at LHC is observed. For $\sqrt{s_{NN}}=200$ GeV, 2.76 TeV and 5.02 TeV the $\langle p_T \rangle^{core}$ and $\sqrt{\frac{dN^{core}}{dy}/(S_{\perp}^{geom})^{core}}$ were estimated based on the core-corona approach. The corresponding $\langle p_T \rangle^{core}$ versus $\sqrt{\frac{dN^{core}}{dy}/(S_{\perp}^{geom})^{core}}$ show lower slopes and their decrease going from $\sqrt{s_{NN}}=200$ GeV to 5.02 TeV is less evident for all three species. This shows the importance of discriminating between the corona and core contributions in such a type of analysis, for a quantitative comparison. The decrease in the slopes from RHIC to LHC for all species and for the most central collisions at LHC energies seems to support the approach presented in Ref. [10]. A much better scaling as a function of $\sqrt{\frac{dN}{dy}/S_{\perp}^{geom}}$ is observed for the slope from the linear fit of the $\langle p_T \rangle$ dependence on the particle mass and the BGBW fit parameter, $\langle\beta_T\rangle$. The offset of the $\langle p_T \rangle$ particle mass dependence and the T_{kin}^{fo} parameter show a clear jump towards larger values between RHIC and LHC energies. As it was already mentioned, other phenomena, like suppression and its azimuthal dependence as well as the hydrodynamic expansion in the deconfined and after hadronization stages, also have to be considered. The very similar dependence of the $\langle p_T \rangle$, $\langle p_T \rangle$ particle mass dependence and the BGBW fit parameter, $\langle\beta_T\rangle$, on $\sqrt{\frac{dN}{dy}/S_{\perp}}$ in pp and Pb-Pb collisions at LHC energies support the assumption that the global properties evidenced at LHC energies are determined by the properties of flux tubes of $\sim 1/\sqrt{\frac{dN}{dy}/S_{\perp}}$ size, the system size playing a minor role.

ACKNOWLEDGMENTS

This work was carried out under the contracts sponsored by the Ministry of Research and Innovation: RONIPALICE-04/16.03.2016 (via IFA Coordinating Agency) and PN-18 09 01 03.

- [1] L.V.Gribov, E.M.Levin and M.G.Ruskin, Phys.Rep. 100 (1983) 1 and references therein
- [2] H1 Collaboration, Nucl.Phys.B 470 (1996) 3
- [3] ZEUS Collaboration, Eur.Phys.J. C7 (1999) 609 and references therein
- [4] H1 Collaboration, Eur.Phys.J. C64 (2009) 561

- [5] L.McLarren and R.Venugopalan, Phys.Rev.D 49 (1994) 2233; Phys.Rev.D 49 (1994) 3352; Phys.Rev.D 50 (1994) 2225
- [6] E.Iancu, A.Leonidov and L.McLarren, Nucl.Phys.A 692 (2001) 583; arXiv:hep-ph/0202270; E.Ferreiro, E.Iancu, A.Leonidov and L.McLarren NPA 703 (2002) 489

- [7] D. Kharzeev, E. Levin and M. Nardi, Nucl.Phys.A 730 (2004) 448; Nucl.Phys.A 743 (2004) 329; D. Kharzeev and E. Levin, Phys.Rev.C 71 (2005) 054903; D. Kharzeev and M. Nardi, Phys.Lett.B 507 (2001) 121; D. Kharzeev, E. Levin and L. McLarren, Nucl.Phys.A 748 (2005) 627; Phys.Lett.B 561 (2003) 93
- [8] Y.L.Dokshitzer, V.A.Khoze and S.Troian, J.Phys.G 17 (1991) 1585
- [9] T. Lappi, Eur.Phys.J. C71 (2011) 1699
- [10] E. Levin and A.H. Rezaeian, Phys.Rev.D 83 (2011) 114001
- [11] CMS Collaboration, JHEP 1009 (2010) 91
- [12] CMS Collaboration, Phys.Lett.B 718 (2013) 795
- [13] ALICE Collaboration, Phys.Lett.B 719 (2013) 29
- [14] ATLAS Collaboration, Phys.Lett.B 725 (2013) 60
- [15] ALICE Collaboration, Nucl.Phys.A 931 (2014) c888
- [16] LHCb Collaboration, EPJ Web of Conferences 141 (2017) 01007
- [17] ALICE Collaboration, Nature Physics 13 (2017) 535
- [18] E. Shuryak and I. Zahed, Phys.Rev.C 88 (2013) 044915
- [19] H. Petersen et al., Phys.Rev.C 78 (2008) 044901
- [20] W.T.Deng, X.N.Wang and R.Xu, Phys.Rev.C 83 (2011) 014915
- [21] R.Andrade et al., Eur.Phys.J. A29 (2006) 23
- [22] J.Xu and C.M.Ko, Phys.Rev.C 84 (2011) 014903
- [23] V.P.Konchakovski et al., Phys.Rev.C 85 (2012) 044922
- [24] T.Pierog et al, Phys.Rev.C 92 (2015) 034906
- [25] T. Sjöstrand, S.Mrenna and P.Z.Skands, JHEP 5 (2006) 26
- [26] J.Bellm et al., Eur.Phys.J. C76 (2016) 196
- [27] F.W.Bopp, R.Engel and J.Ranft, arXiv:hep-ph/9803437
- [28] A. Buckley et al., Phys.Rep. 504(2011)145
- [29] C.Bierlich, G.Gustafson and L. Lönnblad, arXiv:hep-ph/1612.05132
- [30] R.J.Glauber, Phys.Rev. 100 (1955) 242
- [31] V.Franco and R.J.Glauber, Phys.Rev. 142 (1966) 1195
- [32] M.L.Miller et al., Ann.Rev.Nucl.Part.Sci. 57 (2007) 205
- [33] M. Rybczynski, G. Stefanek, W. Broniowski, P. Bozek, Comp. Phys. Comm. 185 (2014) 1759
- [34] STAR Collaboration, Phys.Rev.C 79 (2009) 034909
- [35] ALICE Collaboration, Phys.Rev.C 88 (2013) 044910
- [36] U. Amaldi, 60 Years of CERN Experiments and Discoveries, from www.worldscientific.com
- [37] ALICE Collaboration, Phys.Rev.Lett. 116 (2016) 222302
- [38] L. Adamczyk et al., STAR Collaboration, Phys.Rev.C 96 (2017) 044904
- [39] B.Alver et al., Phys.Rev.C 77 (2008) 014906
- [40] ALICE Collaboration, Nucl.Phys.A 967 (2017) 421
- [41] ALICE Collaboration, R. Pregonella SQM2017
- [42] X. Zhu, STAR Collaboration, CPOD2011
- [43] A.R. Timmins, STAR Collaboration, Strange Quark Matter Conference, Beijing, China, 2008
- [44] STAR Collaboration, Phys.Rev.C 83 (2011) 024901
- [45] STAR Collaboration, Phys.Rev.Lett. 98 (2007) 062301
- [46] ALICE Collaboration, Phys.Rev.Lett. 111 (2013) 222301
- [47] B. Abelev et al., Eur.Phys.Journ. Web of Conference 171(2018)13007
- [48] ALICE Coll., Phys.Rev.C 95 (2017) 064606
- [49] F.Becattini et al., Phys.Rev.C 69 (2004) 024905
- [50] P.Bozek, Acta Phys. Pol. B36 (2005) 3071
- [51] K.Werner, Phys.Rev.Lett. 98 (2007) 152301
- [52] F.Becattini, J.Manninen, J.Phys.G 35 (2008) 104013, Phys.Lett.B 673 (2009) 19
- [53] J.Aichelin, K.Werner, Phys.Rev.C 79 (2009) 064907, J.Phys.G 37 (2010) 094006, Phys.Rev.C 82 (2010) 034906
- [54] P.Bozek, Phys.Rev.C 79 (2009) 054901
- [55] M.Gemard and J.Aichelin, Astron.Nachr. 335 (2014) 660
- [56] M. Petrovici et al., Phys.Rev.C 96 (2017) 014908
- [57] ALICE Collaboration, Eur.Phys.J. C75 (2015) 226
- [58] A.K.Dash, ALICE Collaboration 9th Int. Workshop on MPI at LHC, Dec. 11-15, 2017
- [59] E.Schnedermann et al., Phys.Rev.C 48 (1993) 2462
- [60] X.Sun, H.Masui, A.M.Poskanzer and A.Schman, Larren Phys.Rev.C 91 (2015) 024903
- [61] STAR Collaboration, Phys.Rev.C 93 (2016) 014907
- [62] A.A.Bylinkin and A.A.Rostovtsev, Phys.Atom.Nucl. 75 (2012) 999 (Yad.Fiz. (2012) 1060)
- [63] A.Bzdak, B.Schenke, P.Tribedy and R.Venugopalan, Phys.Rev.C 87 (2013) 064906
- [64] B.Schenke, P.Tribedy and R.Venugopalan, Phys.Rev.C 86 (2012) 034908
- [65] L.McLarren, M.Praszalowicz and B.Schenke, Nucl.Phys.A 916 (2013) 210
- [66] L.McLarren and M.Praszalowicz, Phys.Lett.B 741 (2015) 246
- [67] T.S.Biro, H.B.Nielsen and J.Knoll, Nucl.Phys.B 245 (1984) 449
- [68] FOPI Collaboration, Phys.Rev.Lett. 74 (1995) 5001 and references therein